Inorganic Chemistry

Article

pubs.acs.org/IC

Assembly of Metal–Organic Frameworks Based on 3,3′,5,5′-Azobenzene-tetracarboxylic Acid: Photoluminescences, Magnetic Properties, and Gas Separations

Shaowei Zhang, Jiangong Ma, Xiaoping Zhang, Eryue Duan, and Peng Cheng*

Department of Chemistry, Key Laboratory of Advanced Energy Materials Chemistry (MOE), Nankai University, and Collaborative Innovation Center of Chemical Science and Engineering, Tianjin 300071, P. R. China

Supporting Information

ABSTRACT: We systematically studied the solvothermal reactions of transition-metal ions and H_4abtc ligand and successfully isolated five metal–organic frameworks with various characterized tools, which are formulated as $\{[Mn_2(abtc)(DMA)_{2.75}]\cdot 1.25(DMA)\}_n$ (**1**), $\{[NH_2(CH_3)_2][Co_3(COOH)_{2.5}(abtc)(H_2O)_2]_2\cdot H_2O\}_n$ (**2**), $\{[Zn_3(abtc)_{1.5}(DMF)_3]\cdot 1.75(DMF)\}_n$ (**3**), $\{[Zn_2(abtc)(H_2O)_{0.75}(DMA)_{0.5}]\cdot 3(DMA)\cdot(H_2O)\}_n$ (**4**), and $\{[Cd_2(abtc)(DMA)_2]\cdot 2(DMA)\}_n$ (**5**), (H_4abtc = 3,3′,5,5′-azobenzenetetracarboxylic acid, DMF = *N*,*N*-dimethylformamide, and DMA = *N*,*N*-dimethylacetamide). **1**–**5** all consist of $\{M_n(CO_2)_4\}$-type clusters and H_4abtc ligands; however, they exhibit four distinct architectures resulting from different coordinated modes of H_4abtc ligand. A pair of Mn^{2+}ions in **1** forms a $\{Mn_2(CO_2)_4\}$ cluster, which further results in the "**PtS**"-type three-dimensional (3D) framework. In **2**, three independent Co^{2+} ions are bridged by $COOH^-$ groups to afford a $\{Co_3\}$ core, and $\{Co_3\}$ cores are connected by $abtc^{2-}$ to generate a "**ZSW1**"-type topology. Two types of $\{Zn_2(CO_2)_4\}$ secondary building units in **3** linked by $abtc^{2-}$ give the 3D "**NbO**"-type cage. When DMF is replaced by DMA and CH_3OH, the scarce "**nou**"-type topology of **4** is obtained. And **5** is isomorphous to **1**. Photoluminescence properties of **1**–**5** were characterized. Magnetic measurements demonstrate that dominant antiferromagnetic interactions exist in **1** and **2**. In addition, **3** exhibits significant adsorption capability of CO_2 and highly selective sorption of CO_2 over N_2.

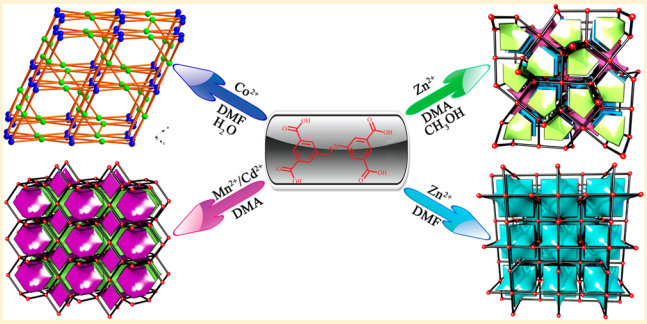

INTRODUCTION

Over the past two decades, the construction of metal–organic frameworks (MOFs) has attracted immense interest because of the intriguing architectures[1] as well as the potential applications in gas separation and storage,[2] chemical sensors,[3] catalysis,[4] and magnetism.[5] To acquire the above purposes, MOFs are expected to have high surface area, large pore size, and high stability. A usual approach for improving the above applications is to introduce linear extension of the rigid bridges to assemble robust frameworks. Nevertheless, employing longer linkers to construct porous MOFs could tend to form interpenetration structures, which decrease the porosity and the void available.[1] Therefore, introducing highly symmetrical organic linkers and suitable metal ions to form porous MOFs with special topologies is of great interest.[1] On the other hand, secondary building units (SBUs) are usually introduced for modularly constructing porous MOFs since they can readily design and predict the final molecular structures. Especially, $\{M_2(CO_2)_4\}$-type paddlewheel SBUs are extensively served for the preparation of porous MOFs, which could be generated by reacting transition metal (M^{2+}) ions and appropriate carboxylic ligands under the solvothermal conditions.[1,6] From this point, the topological concept is an available implement for understanding and further handling the elusive MOFs, which has been widely applied to construct the desired MOFs illustrated by suitable linkers for forming abundant MOFs with various topologies (**nbo**, **pts**, **pcu**, **dia**, **cds**, **srs**, etc.).[7]

In previous investigations, the multidentate organic aromatic polycarboxylate ligands, such as 1,3-benzenedicarboxylate,[8a] 1,3,5-benzenetricarboxylate,[8b] biphenyl-3,4′,5-tricarboxylate,[8c] and 3,3′,5,5′-biphenyltetracarboxylate,[8d] have been proven to be useful linkers in the preparation of MOFs with expectant topologies ascribed to their diverse coordinated modes.[8] In contrast, 3,3′,5,5′-azobenzene-tetracarboxylic acid (H_4abtc), as one kind of connective aromatic tetracarboxylate ligand, possesses many advantages to inspire our research interests:[6,9] (i) The azo bond is well-known photochromic group that could reverse its isomerization between *cis* and *trans* states upon irradiation and other conditions.[10] (ii) The rigid H_4abtc ligand with a longer organic backbone has four carboxyl groups, being easily partially or completely deprotonated to adopt various acidity-dependent binding modes and geometrical configurations to improve the thermal stability and rigidity of the products. (iii) Especially, d^{10} metal ions and the conjugated π

Received: October 11, 2014
Published: December 24, 2014

DOI: 10.1021/ic502488c
Inorg. Chem. 2015, 54, 586–595

Table 1. Crystallographic Data and Structure Refinements for 1−5

	1	2	3	4	5
formula	$C_{128}H_{168}N_{24}O_{48}Mn_8$	$C_{39}H_{35}N_5O_{31}Co_6$	$C_{38.25}H_{42.25}N_{7.75}O_{16.75}Zn_3$	$C_{120}H_{164}N_{22}O_{53}Zn_8$	$C_{32}H_{42}N_6O_{12}Cd_2$
Mr (g mol^{-1})	3250.38	1423.31	1074.66	3285.97	927.53
T (K)	126.8(1)	128.2(1)	128.6(1)	127.9(4)	127.2(1)
cryst syst	monoclinic	orthorhombic	monoclinic	monoclinic	monoclinic
space group	$P2_1/c$	$Pnna$	$I2/c$	$P2_1/c$	$P2_1/c$
a (Å)	14.3400(4)	24.2784(9)	21.7672(5)	10.1591(5)	14.4225(4)
b (Å)	14.0474(4)	13.3684(4)	19.6330(5)	17.6487(7)	14.2601(4)
c (Å)	22.1387(7)	15.9103(6)	29.4028(6)	22.6853(10)	22.5106(7)
β (deg)	100.600(3)	90	99.478(2)	99.592(5)	100.154(3)
V (Å^3)	4383.5(2)	5163.9(3)	12394.0(5)	4010.5(3)	4557.2(2)
Z	1	4	8	1	4
cryst size [mm^3]	0.18 × 0.16 × 0.12	0.20 × 0.12 × 0.08	0.16 × 0.14 × 0.12	0.10 × 0.04 × 0.02	0.20 × 0.12 × 0.10
Dc (g cm^{-3})	1.231	1.827	1.152	0.898	1.225
μ (mm^{-1})	0.633	1.986	1.210	1.225	0.979
R_{int}	0.0301	0.0265	0.0241	0.0526	0.0440
limiting indices	$-16 \le h \le 17$	$-16 \le h \le 28$	$-25 \le h \le 25$	$-12 \le h \le 12$	$-17 \le h \le 17$
	$-16 \le k \le 16$	$-15 \le k \le 15$	$-23 \le k \le 22$	$-20 \le k \le 18$	$-16 \le k \le 16$
	$-26 \le l \le 26$	$-18 \le l \le 12$	$-20 \le l \le 34$	$-20 \le l \le 26$	$-26 \le l \le 26$
reflns collected	21 657	14 841	22 642	16 677	35 167
indep reflns	7662	4512	10 743	6963	7969
params	736	403	682	333	536
GOF on F^2	1.049	1.148	1.098	0.914	1.124
R_1, wR_2 [$I > 2\sigma(I)$]	0.0563, 0.1482	0.0573, 0.1426	0.0458, 0.1298	0.0688, 0.1702	0.0721, 0.1701
R_1, wR_2 [all data]	0.0636, 0.1550	0.0606, 0.1448	0.0527, 0.1349	0.1020, 0.1875	0.0765, 0.1728

systems including aromatic rings are beneficial to exploit luminescence materials.

On the basis of the above considerations and our previous work, H_4abtc is chosen to elaborate new MOFs. By adjusting the types of M^{2+} ions and the solvents and/or reaction temperature by solvothermal methods, we herein report the syntheses and structures of five three-dimensional (3D) MOFs, namely, $\{[Mn_2(abtc)(DMA)_{2.75}]\cdot 1.25(DMA)\}_n$ (**1**), $\{[NH_2(CH_3)_2][Co_3(COOH)_{2.5}(abtc)(H_2O)_2]_2\cdot H_2O\}_n$ (**2**), $\{[Zn_3(abtc)_{1.5}(DMF)_3]\cdot 1.75(DMF)\}_n$ (**3**), $\{[Zn_2(abtc)(H_2O)_{0.75}(DMA)_{0.5}]\cdot 3(DMA)(H_2O)\}_n$ (**4**) and $\{[Cd_2(abtc)(DMA)_2]\cdot 2(DMA)\}_n$ (**5**), (DMF = *N*,*N*-dimethylform-amide, DMA = *N*, *N*-dimethylacetamide). **1**−**5** are all constructed by $\{M_n(CO_2)_4\}$-type SBUs and $abtc^{2-}$ ligands; however, they present four distinct structures resulting from different coordinated modes of $abtc^{2-}$ ligands. A pair of Mn^{2+} centers in **1** forms a $\{Mn_2(CO_2)_4\}$ cluster, and adjacent $\{Mn_2(CO_2)_4\}$ clusters further result in the 3D network with "**PtS**"-type topological structure via the $abtc^{2-}$ linkers. In **2**, three crystallographically independent Co^{2+} ions are bridged by $COOH^-$ groups to afford a $\{Co_3\}$ core, and the $\{Co_3\}$ cores are linked by $abtc^{2-}$ ligands to present the 3D framework with a new "**ZSW1**"-type topological structure. Two types of paddlewheel-shaped $\{Zn_2(CO_2)_4\}$ cluster SBUs in **3** linked by $abtc^{2-}$ ligands give the 3D "**NbO**"-type cage. Unlike **3**, when DMF is replaced by DMA and CH_3OH, the scarce "**nou**"-type topological architecture of **4** is obtained. And **5** displays the same topology structure as **1**. The solid-state photoluminescence properties of **1**−**5** were examined. Furthermore, variable-temperature magnetic susceptibility measurements of **1** and **2** were studied. In addition, gas sorption and separation of **3** was evaluated as well.

EXPERIMENTAL SECTION

General Methods and Materials. The H_4abtc ligand was prepared according to the previous report developed by Ameerunisha et al. for 4,4′-azobenzoic acid[11] and was further characterized by ^{1}H NMR. Other reagents were used without further treatment. Elemental analyses (C, H, and N) were measured on a PerkinElmer 2400-IICHNS/O analyzer. Thermogravimetric analyses (TGA) were conducted on a Labsys NETZSCH TG 209 Setaram apparatus under a N_2 atmosphere from 25 to 800 °C with the rate of 10 °C·min^{-1}. The emission spectra were obtained on a Varian Cary Eclipse Fluorescence spectrophotometer. The solid-state UV−vis spectra were recorded with a JASCO V-570 spectrophotometer at the ambient temperature. PXRD spectra were performed on a Rigaku Ultima IV instrument with Cu Kα radiation (λ = 1.540 56 Å), in the range 2θ = 3−60° with the scan speed of 10° min^{-1}. Magnetic data were measured on a Quantum Design SQUID VSM magnetometer. Diamagnetic corrections were taken with sample holder and Pascal's constants. The ^{1}H NMR spectrum was tested on a Mercury Vx-300 NMR spectrometer.

Synthesis of $\{[Mn_2(abtc)(DMA)_{2.75}]\cdot 1.25(DMA)\}_n$ (1). A mixture of $MnCl_2\cdot 4H_2O$ (0.0792 g, 0.40 mmol), H_4abtc (0.0358 g, 0.10 mmol), and DMA (5.0 mL) was sealed in a 20 mL screw-capped vial and placed in an oven at 120 °C for 72 h, and then the mixture was cooled to room temperature over a period of 48 h. Yellow block crystals were collected by filtering, washed with DMA, and dried. Yield: ca. 85% (based on H_4abtc). Anal. Calcd (%) for $C_{32}H_{42}N_6O_{12}Mn_2$: C 47.30, H 5.21, N 10.34. Found: C 47.17, H 5.32, N 10.15.

Synthesis of $\{[NH_2(CH_3)_2][Co_3(COOH)_{2.5}(abtc)(H_2O)_2]_2\cdot H_2O\}_n$ (2). H_4abtc (0.0179 g, 0.05 mmol), $Co(NO_3)_2\cdot 6H_2O$ (0.0433 g, 0.15 mmol), HNO_3 (0.10 mL), 1 mol·L^{-1} LiOH (0.10 mL), DMF (2.5 mL), and H_2O (1.5 mL) were successively added in a 25 mL Telfon-lined stainless steel autoclave. The resulting mixture was stirred for 10 min, kept at 140 °C for 72 h, and then slowly cooled to 40 °C in 48 h. Red bock crystals were collected by filtering and dried in air. Yield: ca. 80% (based on H_4abtc). Anal. Calcd (%) for $C_{39}H_{35}N_5O_{31}Co_6$: C 32.91, H 2.48, N 4.92. Found: C 32.75, H 2.51, N 4.78.

Synthesis of $\{[Zn_3(abtc)_{1.5}(DMF)_3]\cdot 1.75(DMF)\}_n$ (3). A mixture of $Zn(NO_3)_2\cdot 6H_2O$ (0.0892 g, 0.30 mmol), H_4abtc (0.0358 g, 0.10 mmol), and DMF (2.5 mL) was sealed in a 20 mL vial and placed in

DOI: 10.1021/ic502488c
Inorg. Chem. 2015, 54, 586−595

an oven at 100 °C for 15 h. Yellow block crystals were harvested by filtering, washed with DMF and dried. Yield: ca. 90% (based on H_4abtc). Anal. Calcd (%) for $C_{38.25}H_{42.25}N_{7.75}O_{16.75}Zn_3$: C 42.75, H 3.96, N 10.10. Found: C 42.53, H 4.19, N 10.02.

Synthesis of $\{[Zn_2(abtc)(H_2O)_{0.75}(DMA)_{0.5}]\cdot 3(DMA)\cdot(H_2O)\}_n$ (4). A mixture of $Zn(NO_3)_2\cdot 6H_2O$ (0.1190 g, 0.40 mmol), H_4abtc (0.0358 g, 0.10 mmol), HNO_3 (0.010 mL), DMA (4.0 mL), and CH_3OH (1.0 mL) was enclosed in a 20 mL screw-capped vial, put in an oven at 100 °C for 72 h, and then the mixture was cooled to room temperature over a period of 48 h. Yellow strip crystals were collected by filtering, washed with DMA, and dried in air. Yield: ca. 86% (based on H_4abtc). Anal. Calcd (%) for $C_{30}H_{41}N_{5.5}O_{13.25}Zn_2$: C 43.86, H 5.03, N 9.38. Found: C 43.98, H 5.12, N 9.49.

Synthesis of $\{[Cd_2(abtc)(DMA)_2]\cdot 2(DMA)\}_n$ (5). The synthesis process of **5** was similar to that of **4**, except that $Cd(NO_3)_2\cdot 4H_2O$ (0.1234 g, 0.40 mmol) was used instead of $Zn(NO_3)_2\cdot 6H_2O$. Yield: ca. 92% (based on H_4abtc). Anal. Calcd (%) for $C_{32}H_{42}N_6O_{12}Cd_2$: C 41.44, H 4.56, N 9.06. Found: C 41.49, H 4.48, N 9.09.

X-ray Crystallography. Single-crystal data for **1**−**5** were obtained on an Oxford SuperNova diffractometer with graphite monochromatic Mo Kα radiation (λ = 0.710 73 Å) at 128 K. Routine Lorentz polarization and empirical absorption corrections were used. The structures were resolved by direct methods and refined by full−matrix least-squares methods on F^2 with the SHELXTL-97 program package.[12] Anisotropic thermal parameters were assigned to all non-H atoms. Positions of H atoms linked to C and N atoms were geometrically placed. All H atoms were refined isotropically as a riding mode using the default parameters. The disorder DMA, DMF, and $[NH_2(CH_3)_2]^+$ molecules were geometrically restrained. For **1**, the C, N, and O atoms from two coordinated DMA molecules and two free DMA molecules display positional disorders, and the relative ratios for C21−C25, C22−C26, C23−C27, C24−C28, N4−N5, and O8−O9 are refined to 0.5/0.5; C29−C33, C30−C34, C36−C32, C35−C31, N6−N7, O11−O10, and C38−C39, C40−C41, C42−C43, and O14−O15 are refined to 0.5/0.25; C45−C48, C46−C50, N9−N10, and O16−O17 are refined to 0.25/0.25, respectively. In the case of **2**, one C atom from the $[NH_2(CH_3)_2]^+$ molecule presents positional disorder, and the relative ratio for C21−C22 is refined to 0.25/0.25. For **3**, C and N atoms from a coordinated DMF molecule show positional disorders, and the relative ratios for C27−C28, C1A−C31, and N5−N6 are refined to 0.667/0.333. For **4**, one O atom from a coordinated DMA shows positional disorder, and the relative ratio for O9−O10 is refined to 0.2/0.3. Although the electron densities of some guest solvents were detected, attempts to define the highly disordered guests were unsuccessful. As a result, the SQUEEZE routine of PLATON[13] was applied to remove the diffraction contribution from guests to give a set of solvent-free diffraction intensities. SQUEEZE estimated a total count of 322 electrons per unit cell. According to the final formula, which was calculated from elemental analyses and TG analyses, these electrons were assigned to be three DMF and one H_2O molecules. As for **5**, a large amount of spatially delocalized electron density in the lattice is found from which two half-dissociated DMA solvent molecules could be identified. However, the remaining electron density is seriously disordered, and attempts to fix the half DMA are unsuccessful. Thus, the final numbers of the solvent are confirmed by element analyses and TG analyses. The final formulas of **1**−**5** were checked by combining single-crystal data, elemental analyses, and TG analyses. The crystallographic data and structural refinements for **1**−**5** are gathered in Table1. Additional crystallographic data are available in the Supporting Information.

Low-Pressure Sorption Experiments. All gas-sorption measurements were evaluated on a Quantachrom IQ_2 automatic volumetric instrument. All gases applied were of 99.999% purity. The as-prepared **3** was immersed in CH_2Cl_2 for 3 d and then degassed at 75 °C for 12 h on degassing station to remove the guest molecules. Large bulb cell (9 mm, from Quantachrome) was loaded with degassed sample of 476 mg to use for gas-sorption experiments. The CO_2 sorption isotherm at 195 K was recorded using a dry ice/acetone bath in the pressure range of 10^{-3}−1 bar. And the CO_2 and N_2 sorption isotherms at 273 and 298 K were tested in a temperature-controlled water bath in the pressure range from 10^{-3} to 1 bar. To evaluate the adsorption selectivity abilities of **3** toward different gases between CO_2 and N_2, the ideal adsorbed solution theory (IAST)[14] selectivity is calculated based on the single gas adsorption data.

RESULTS AND DISCUSSION

Structural Descriptions. The as-synthesized PXRD patterns for **1**−**5** are in good agreement with the simulated PXRD patterns from the single-crystal data, indicating high phase purity for **1**−**5** (Supporting Information, Figure S1). The different intensity may be attributed to the variation in preferred orientation of samples. Besides, bond-valence sum calculations[15] suggest that all Mn ions in **1** and Co ions in **2** are in the +2 oxidation states, respectively.

X-ray crystallographic analysis demonstrates that **1** belongs to the monoclinic space group $P2_1/c$, with two independent Mn ions, one abtc^{4-} ligand, 2.75 coordinated DMA molecules, and 1.25 free DMA molecules in the asymmetric unit (Figure 1a),

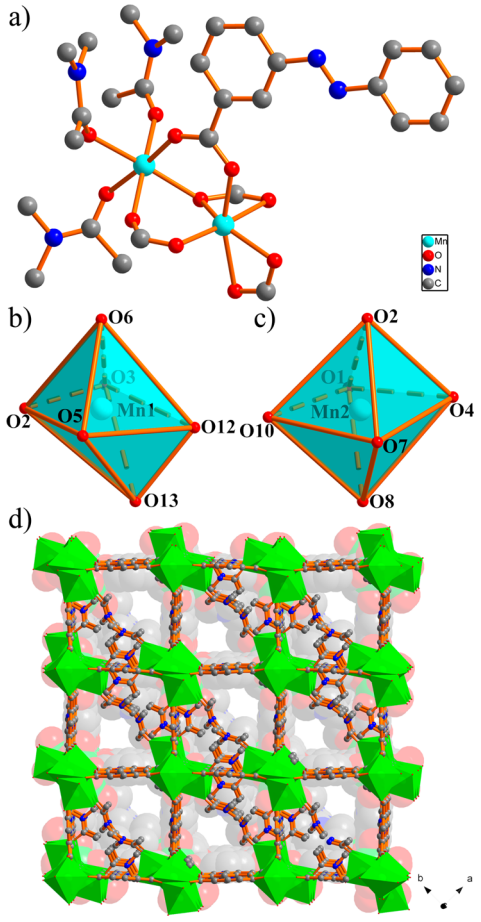

Figure 1. (a) Ball-and-stick representation of the structural unit of **1**. (b, c) The coordination environments of Mn ions. (d) The 3D framework of **1**. H and free DMA molecules are omitted for clarity.

giving rise to the formula $\{[Mn_2(abtc)(DMA)_{2.75}]\cdot 1.25(DMA)\}_n$ (**1**). Mn1 adopts six-coordinated distorted octahedral geometry with six O from three carboxylate groups of four abtc^{4-} ligands: two bidentate and one chelating/bridging tridentate [Mn−O: 2.093(2)−2.491(2) Å] (Figure 1b). Mn2 displays the same geometry as that of the Mn1, which is defined by three terminal O of DMA molecules [Mn−O: 2.105(2)−2.188(8) Å], while the other three O are from three abtc^{4-}

DOI: 10.1021/ic502488c
Inorg. Chem. 2015, 54, 586−595

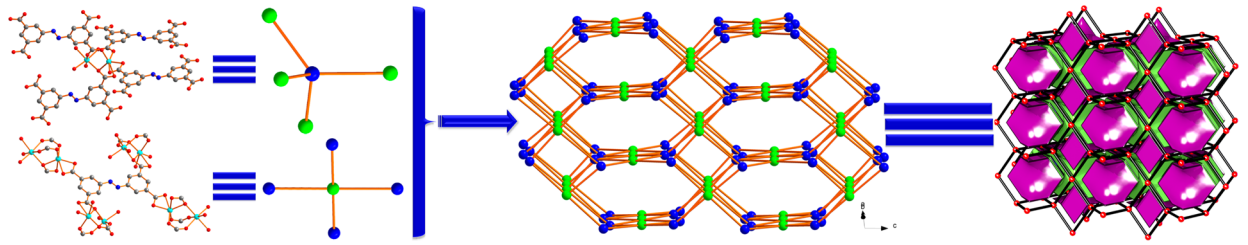

Figure 2. (left, center) A schematic view of the (4, 4)-connected net for **PtS**-type topology framework presented by **1**. (right) The tiling.

ligands [Mn−O: 2.137(2)−2.197(2) Å] (Figure 1c). Mn1 and Mn2 ions are connected by abtc^{4-} ligands to give $\{Mn_2(CO_2)_4\}$ clusters, with the distance of Mn ··· Mn being 3.479 Å. The isophthalate group of the abtc^{4-} ligand acts as a tetrakis-(monodentae) linker, which is bound to each side to two $\{Mn_2(CO_2)_4\}$ clusters through the carboxylate O in a *syn*−*syn* configuration producing one-dimensional (1D) chains that run parallel to the *a* and *b* axes, respectively. The abtc^{4-} ligand is coplanar and serves as a rectangular building unit. Each abtc^{4-} is surrounded with four $\{Mn_2(CO_2)_4\}$ clusters, and each $\{Mn_2(CO_2)_4\}$ cluster is connected by four abtc^{4-} ligands, which extend infinitely to generate the 3D framework. There are open rectangular channels of approximately 10.0 × 10.2 Å along the *c* axis (Figure 1d), which are occupied by 2.75-coordinated DMA molecules and 1.25 free DMA molecules, as established by combining single-crystal structures, elemental analyses, and TG analyses. The void volume for **1** with and without coordinated DMA is 32.1% and 65.3% (excluding free DMA molecules), respectively, as calculated by PLATON.[13]

To know the structure of **1** more clearly, the topology of **1** is acquired by using the freely available program TOPOS.[16] If the H_4abtc ligands act as linkers and the $\{Mn_2(CO_2)_4(DMA)_{2.75}\}$ clusters serve as four-connected nodes, the 3D framework of **1** can be presented as a (4, 4)-connected **PtS**-type topology (Figure 2).

The solvothermal reaction of $Co(NO_3)_2{\cdot}6H_2O$ and H_4abtc in the mixed solvent of DMF/H_2O generates red block crystals of **2**. Complex **2** belongs to the orthorhombic space group *Pnna*. The structural unit of $\{[NH_2(CH_3)_2][Co_3(COOH)_{2.5}(abtc)(H_2O)_2]_2{\cdot}H_2O\}_n$ (**2**) consists of two $\{Co_3\}$ cores, one abtc^{4-} ligand, 2.5 $COOH^-$ groups, two coordinated H_2O molecules (Figure 3a), two $[NH_2(CH_3)_2]^+$ ions, and one free H_2O molecule. Three independent Co ions present six-coordinated distorted octahedral geometries (Supporting Information, Figure S2). Co1 is arranged by three O from two abtc^{4-} ligands; two O are from two $COOH^-$ groups, and one O is from a water molecule [Co−O: 2.020(4)−2.192(4) Å]. The Co2 ion is bonded to four O from four abtc^{4-} ligands and two O from two $COOH^-$ groups [Co−O: 2.046(4)−2.196(4) Å], while the coordinated environment of Co3 is similar to that of Co1, being surrounded by three O from two abtc^{4-} ligands, two O from two $COOH^-$ groups and one O from a water molecule [Co−O: 2.043(5)−2.212(3) Å]. Interestingly, Co1 and Co2 via an edge-sharing mode and Co2 and Co3 through a vertex-sharing mode form the $\{Co_3\}$ cluster. To the best of our knowledge, this type of $\{Co_3\}$ cluster has not been reported, which is significantly distinguished from the linear trimer and triangular cluster documented.[9d,17] Adjacent trimeric $\{Co_3\}$ clusters can be linked by $COOH^-$ groups to produce the $\{Co_6\}$ dimers (Figure 3b), further resulting in the 1D helical chain (Figure 3c). Adjacent chains

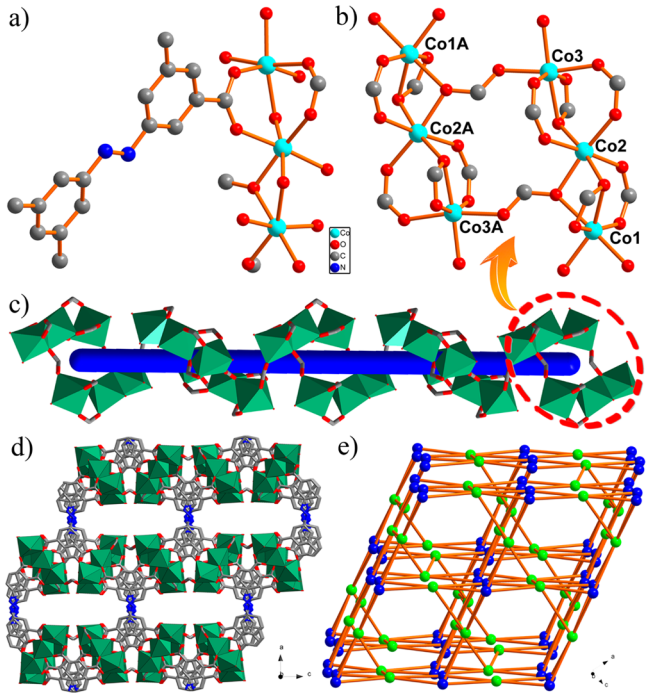

Figure 3. (a) Ball-and-stick representation of the structural unit of **2**. (b) The dimeric $\{Co_6\}$ SBU bridged by $COOH^-$ groups. (c) The 1D helical chain constructed from $\{Co_6\}$ SBUs and $COOH^-$ groups. (d) The 3D framework of **2**. (e) A schematic view of the (4, 6)-connected net for **ZSW**-type topology framework exhibited by **2**. H, free H_2O, and $[NH_2(CH_3)_2]^+$ molecules are omitted for clarity.

are bridged by abtc^{4-} ligands to produce the 3D framework (Figure 3d).

Topologically, each $\{Co_3\}$ cluster acts as a six-connected node, while the H_4abtc ligand serves as a linker; the 3D structure of **2** can act as a (4, 6)-connected topology with the Schläfli symbol of $\{3{\cdot}4^5\}\{3^2{\cdot}4^2{\cdot}6^4{\cdot}7^7\}$ (Figure 3e), which is a new topology named as **ZSW1**.[16]

In the case of $\{[Zn_3(abtc)_{1.5}(DMF)_3]{\cdot}1.75(DMF)\}_n$ (**3**), it belongs to the monoclinic space group *I*2/*c*. The asymmetric unit contains three independent Zn ions, 1.5 abtc^{4-} ligands, three coordinated DMF molecules (Figure 4a), and 1.75 free DMF molecules. Three independent Zn ions exhibit five-coordinated square pyramid geometries (Supporting Information, Figure S3). Zn1 and Zn2 ions in **3** are connected by four bridging carboxylates to produce a paddlewheel-shaped $\{Zn_2(CO_2)_4\}$ SBU, while Zn3 and its symmetric ion generate another paddlewheel $\{Zn_2(CO_2)_4\}$ SBU. Each paddlewheel $\{Zn_2(CO_2)_4\}$ SBU is connected by four carboxylate groups from four different abtc^{4-} ligands, and each Zn ion is also bound to a DMF molecule at the axial site of the paddlewheel SBU. Interestingly, six abtc^{4-} ligands bridge six pairs of

DOI: 10.1021/ic502488c
Inorg. Chem. 2015, 54, 586−595

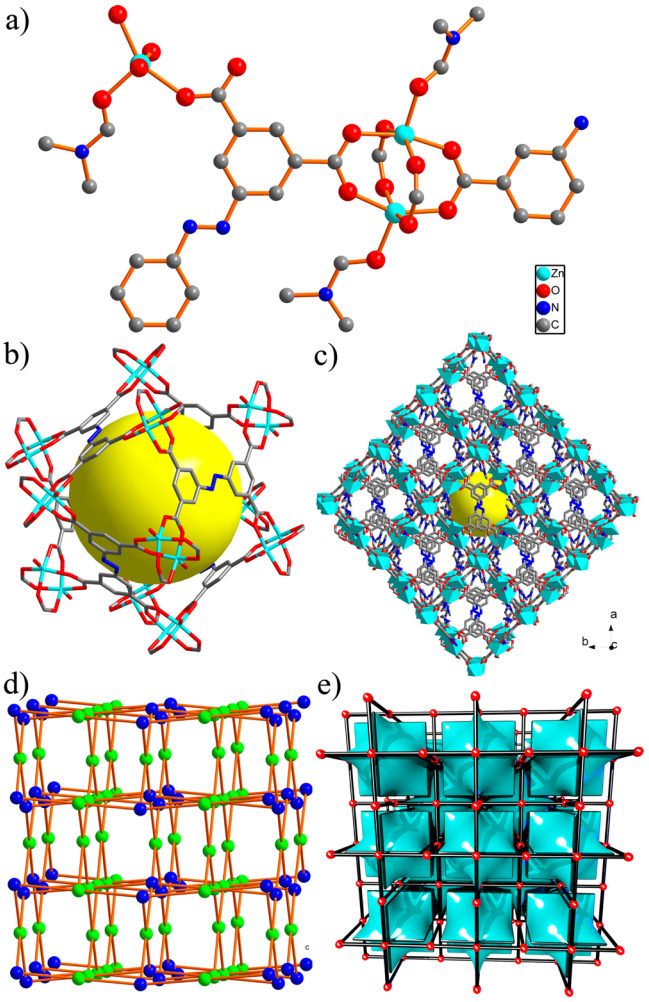

Figure 4. (a) Ball-and-stick representation of the structural unit of **3**. (b) The cage built by paddlewheel $\{Zn_2(CO_2)_4\}$ SBUs and $abtc^{4-}$ ligands. (c) The 3D framework of **3**. (d) A schematic view of the four-connected net for **NbO**-type topology in **3**. (e) The tiling schematic of **3**. H and coordinated and free DMF molecules are omitted for clarity.

$\{Zn_2(CO_2)_4\}$ SBUs to generate an octahedral cage with a cavity with a diameter of ca. 13.0 Å (Figure 4b), which is filled with coordinated and uncoordinated DMF molecules and thus reduce the space available. Adjacent cages are further connected by $abtc^{4-}$ ligands, leading to an extended **NbO**-type 3D network (Figure 4c–e). Since **3** is noninterpenetrated, high void can be promised. The solvent-accessible volume is 23.3%, calculated using PLATON,[13] whereas the void volume of **3** with and without coordinated DMF is 45.9% and 66.4% (except the free DMF molecules), respectively, as estimated by PLATON.[13]

When DMF solvent for the synthesis of **3** is replaced with DMA and CH_3OH, pure yellow strip crystals $\{[Zn_2(abtc)(H_2O)_{0.75}(DMA)_{0.5}]\cdot 3(DMA)(H_2O)\}_n$ (**4**) are harvested. X-ray single-crystal diffraction analysis indicates that **4** crystallizes in the monoclinic space group $P2_1/c$. The asymmetric unit contains of two independent Zn ions, one $abtc^{4-}$ ligand, 0.5-coordinated DMA, and 0.75-coordinated H_2O molecules (Figure 5a), as well as three free DMA molecules and one free H_2O molecule. The H_2O molecules observed in the structure might come from the highly hydroscopic $Zn(NO_3)_2\cdot 6H_2O$ salts. Two independent Zn ions exhibit different coordinated geometries. Five-coordinated Zn1 atom displays

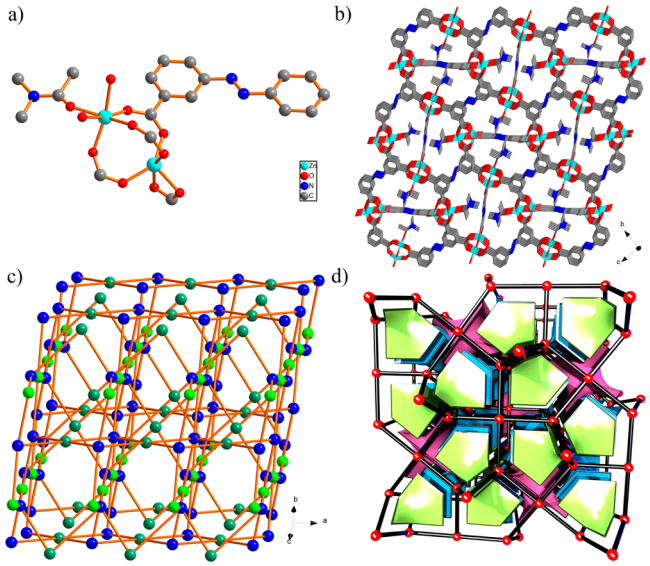

Figure 5. (a) Ball-and-stick representation of the molecular structural unit of **4**. (b) The 3D framework of **4**. (c) A schematic of the (4,4,4)-connected net for **nou**-type topology framework exhibited by **4**. (d) The schematic of **4** shown as tiling. H, free H_2O, and DMA molecules are omitted for clarity.

a trigonal bipyramid geometry with five O from four carboxylate groups of four $abtc^{4-}$ ligands: three bidentate and one chelating linkers [Zn–O: 1.939(4)–2.396(3) Å] (Supporting Information, Figure S4a), whereas Zn2 ion exhibits a six-coordinated distorted octahedral geometry (Supporting Information, Figure S4b), which is defined by three O from three bidentate $abtc^{4-}$ ligands, one O from DMA and two O from water molecules [Zn–O: 1.927(5)–2.327(2) Å]. A pair of Zn ions are connected by four different carboxylates of four independent $abtc^{4-}$ linkers, generating the $\{Zn_2(CO_2)_4(H_2O)_{0.75}(DMA)_{0.5}\}$ SBU, which is further connected by $abtc^{4-}$ linkers to give the 3D structure (Figure 5b). From the topological point of view, taking the $\{Zn_2(CO_2)_4(H_2O)_{0.75}(DMA)_{0.5}\}$ SBU as four-connected node and H_4abtc ligands as linkers, the 3D structure of **4** can be shown as a (4, 4, 4)-connected network with the Schläfli symbol of $\{4\cdot 6^5\}_2\{4^2\cdot 8^4\}\{6^4\cdot 8^2\}$ (Figure 5c,d), which corresponds to **nou**-type topology and is rare for 3D CPs.[16]

$\{[Cd_2(abtc)(DMA)_2]\cdot 2(DMA)\}_n$ (**5**) is isomorphous to **1**, and the structure skeleton of **5** is similar to that of **1**, except for the numbers of coordinated and free DMA molecules.

All five complexes are prepared by reactions of M^{2+} ions and H_4abtc ligands under solvothermal conditions. According to the above structural analyses, it can be known that the bridged modes of $abtc^{2-}$ ligands (Scheme 1) and the coordination geometries of metal ions are different in five complexes, which results in the diverse structures of the five compounds. Generally, the circuit symbols Schläfli (vertex) notations could be taken to present topologies and promote comparison of structures of distinct components.[16] Since **1** and **5** are isomorphous, only **1** is taken for comparison here. Topological analyses of **1**–**4** by checking the schematic presentations of their chemical connectivity facilitate the depiction and contrast of four different 3D MOFs. **1**, **3**, and **4** contain the $\{M_2(CO_2)_4\}$ SBU and H_4abtc ligands; each $abtc^{4-}$ ligand acts as a rectangular building block and is linked with four $\{M_2(CO_2)_4\}$ SBU, and each $\{M_2(CO_2)_4\}$ SBU is connected

DOI: 10.1021/ic502488c
Inorg. Chem. 2015, 54, 586–595

Scheme 1. 1 and 5: (a), (b); 2: (c); 3: (a), (d); 4: (a), (e)[a]

[a]Coordination modes of $abtc^{2-}$ ligands are observed in **1**−**5**.

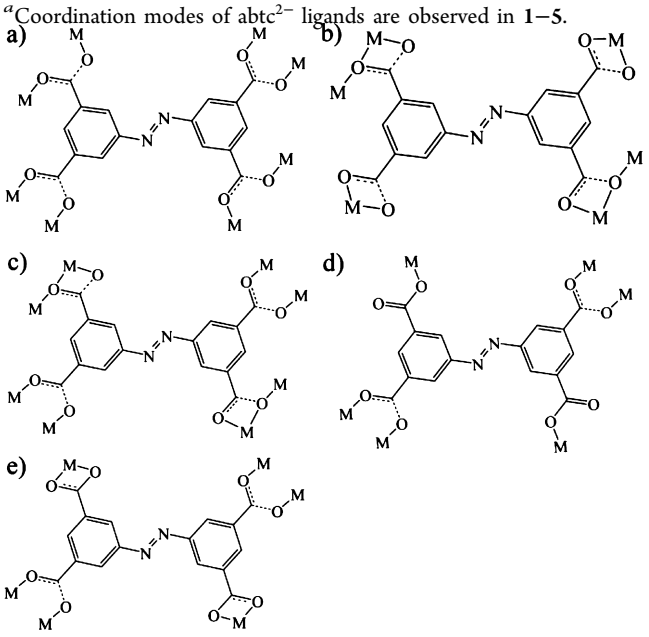

by four $abtc^{4-}$ ligands. Because $abtc^{4-}$ ligands adopt different coordinated modes (Scheme 1), various topological structures are presented in these three compounds. For **2**, three independent Co ions are connected by four $abtc^{4-}$ ligands to give $\{Co_3(CO_2)_4\}$ SBU. Each $\{Co_3(CO_2)_4\}$ cluster is bridged by six rectangular $abtc^{4-}$ ligands, and each $abtc^{4-}$ linker is embraced with four $\{Co_3(CO_2)_4\}$ clusters, which extends infinitely to generate the (4,6)-net 3D framework.

UV−vis Spectra and Photoluminescence Properties. The solid-state UV−vis spectra of **1**−**5** are recorded in the crystalline state at ambient temperature (Supporting Information, Figure S5a). The UV−vis spectra of **1**−**5** all exhibit three broad absorption bands centered at ca. 290, 350, and 460 nm, respectively. The observed main peaks may be attributed to the ligand-based $\pi \rightarrow \pi^*$ or $n \rightarrow \pi^*$ transitions including the −N=N− based $\pi \rightarrow \pi^*$ transition. Similar phenomena have been encountered for earlier MOFs prepared containing azo groups.[18] For **2**, besides the three absorption bands centered at ca. 290, 350, and 460 nm, the band at ca. 685 nm can be assigned as the d−d transition of Co^{II} ion. In contrast, the UV−vis spectrum of the free H_4abtc ligand presents three analogous broad bands at ca. 279, 341, and 455 nm, respectively (Supporting Information, Figure S5a). The coordination of H_4abtc ligand to the metal ion does not seem to affect these ligand-specific transitions in **1**−**5** substantially except for some minor shifts.

MOFs with a d^{10} configuration (such as Zn^{2+} and Cd^{2+}) have been proven to present photoluminescent properties, and the conjugated π systems including aromatic rings are suitable for the exploitation of photoluminescent materials.[3,9e,f] In the case of **3**−**5**, the $abtc^{4-}$ ligand, which has π-conjugated systems that simultaneously bind with the d^{10} center metals, may be excellent candidate for fluorescent materials. As a result, the solid-state photoluminescence properties of **3**−**5** were characterized at ambient temperature on powered sample (Supporting Information, Figure S5b). **3**−**5** all exhibit obvious photoluminescence with two maximum emissions at ca. 395 and 493 nm upon excitation at 310 nm, whereas the free H_4abtc ligand presents similar emissions at ca. 388 and 493 nm (λ = 310 nm). The results suggest that these emission bands of **3**−**5** are neither ligand-to-metal charge transfer (LMCT) nor metal-to-ligand charge transfer (MLCT) in nature because Zn^{2+} and Cd^{2+} ions are tough to reduce or to oxidize due to their d^{10} configuration but rather could be chiefly attributed to an intraligand emission state, which is similar to previous reports.[9e,f] To verify the results, the emission spectra of **1** and **2** were also examined at the same conditions. As depicted in Figure S5b, both **1** and **2** show similar luminescence signs with the emission bands at ca. 393 and 493 nm, which further demonstrates that the emissions signs are derived from $\pi \rightarrow \pi^*$ and/or $n \rightarrow \pi^*$ transitions of the H_4abtc ligand. The emissions of **1**−**5** are quite similar as the free ligand transitions; however, the intensities of **1**−**5** are much weaker than the free ligand, which is attributable to the variation of M^{2+} and the coordination geometries around them since the luminescence behavior is closely related to M^{2+} centers and the ligands bridged to them.[9e,f] These observations indicate that **1**−**5** could find applications as potential fluorescent porous materials. In addition, the expected emission signals coming from the vibronic characters of Zn^{2+} and Cd^{2+} ions are not detected and are hidden by the emission spectra of the organic ligands containing azo function groups in the region of 400−700 nm, which has also been encountered in our previous work.[10]

Magnetic Properties. The direct-current (dc) magnetic susceptibility measurements of **1** and **2** are recorded in the range of 1.8−300 K at an applied magnetic field of 1000 Oe, as shown in Figure 6.

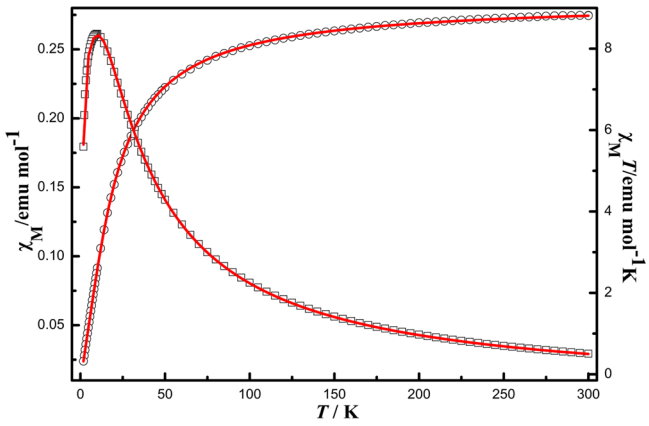

Figure 6. (a) Temperature dependence of magnetic susceptibility in the forms of $\chi_M T$ and χ_M vs T for **1** at an applied field of 1000 Oe between 1.8 and 300 K. The red solid lines represent the best fitting results.

For **1**, the effective $\chi_M T$ per two Mn^{2+} ions is 8.82 $cm^3 \cdot K \cdot mol^{-1}$ at 300 K, which is close to the spin-only value of two uncoupled high-spin Mn^{2+} ions (8.76 $cm^3 \cdot K \cdot mol^{-1}$, $^6S_{5/2}$, g = 2).[19] As the temperature is decreased, $\chi_M T$ decreases smoothly from 300 to 60 K, then decreases dramatically and reaches the minimum value of 0.32 $cm^3 \cdot K \cdot mol^{-1}$ at 1.8 K (Figure 6); the decrease in $\chi_M T$ may be ascribed to the antiferromagnetic interaction between adjacent Mn^{2+} ions. As described in the crystal structures part, adjacent Mn^{2+} ions are connected by a COO^- group to the $\{M_2(CO_2)_4\}$ SBU, and the $Mn^{2+} \cdots Mn^{2+}$ distance is 3.479 Å, much shorter than the distances between adjacent two Mn^{2+} ions bridged by two COO^- groups of the isophthalate group of the $abtc^{4-}$ ligand (longer than 8.28 Å).

DOI: 10.1021/ic502488c
Inorg. Chem. 2015, 54, 586−595

And the single-ion zero-field splitting D and rhombic splitting parameter E for Mn^{2+} ion are small and could be ignored.[19] Therefore, we tried to interpret this magnetic system of **1** by use of the Heisenberg–Dirac–Van Vleck $S_A = S_B = 5/2$ spin-coupled dimer model ($H = -JS_AS_B$).[20]

$$\chi_M' = \frac{2Ng^2\beta^2}{kT}\frac{A}{B} \quad (1)$$

$$A = e^x + 5e^{3x} + 14e^{6x} + 30e^{10x} + 55e^{15x}$$

$$B = 1 + 3e^x + 5e^{3x} + 7e^{6x} + 9e^{10x} + 11e^{15x}$$

In eq 1, N, β, k, and g have their default meanings, $x = J/kT$, and J is the exchange coupling constant within the adjacent Mn^{2+} dimer bridged by the same COO^- group. A molecular field (zJ')[21] representing intrachain Mn^{2+} ions magnetic interactions was added as needed to the actual essence of complex **1**. Therefore, the equation for the magnetic susceptibility of **1** becomes

$$\chi_M = \chi_M'/[1 - 2zJ'\chi_M/Ng^2\beta^2] \quad (2)$$

The best least-squares fit parameters are $g = 2.04$, $J = -2.44$ cm^{-1}, $zJ' = -0.23$ cm^{-1}, and $R = \sum[(\chi_MT)_{obsd} - (\chi_MT)_{calcd}]^2/\sum[(\chi_MT)_{obsd}]^2 = 3.97 \times 10^{-7}$. The negative J value suggests the antiferromagnetic exchange interaction within the Mn^{2+} dimer, and the zJ' value also indicates weakly antiferromagnetic interactions. Furthermore, the curve of χ_M^{-1} versus T in the range of 20–300 K obeys the Curie–Weiss law with $C = 9.34$ $cm^3\cdot K\cdot mol^{-1}$ and $\theta = -16.56$ K (Supporting Information, Figure S6), which further supports the occurrence of a weak antiferromagnetic coupling between adjacent Mn^{2+} ions in **1**.

For **2**, the observed χ_MT value at room temperature is 17.84 $cm^3\cdot K\cdot mol^{-1}$ at 300 K, being larger than the spin-only value of six uncoupled high-spin Co^{2+} ions (11.22 $cm^3\cdot K\cdot mol^{-1}$, $^4F_{9/2}$, $g = 2$), which can be ascribed to the obvious orbital contribution of six-coordinated Co^{2+} ion and is well-known to be pronounced in octahedral field. Such phenomenon has been continually encountered in previously reported Co-containing compounds.[22] The χ_mT steadily decreases with decreasing temperature to reach a minimum value of 3.46 $cm^3\cdot K\cdot mol^{-1}$ at 1.8 K (Figure 7). The decrease of χ_MT value could be attributed to the antiferromagnetic interaction and/or zero-field splitting (ZFS) effects.[22] The curve of χ_M^{-1} versus T above 50 K can be fitted by the Curie–Weiss law, to give $C = 19.18$ $cm^3\cdot K\cdot mol^{-1}$ and $\theta = -21.99$ K (Supporting Information, Figure S7); the large and negative θ value imply the existence of antiferromagnetic coupling in **2**.[22]

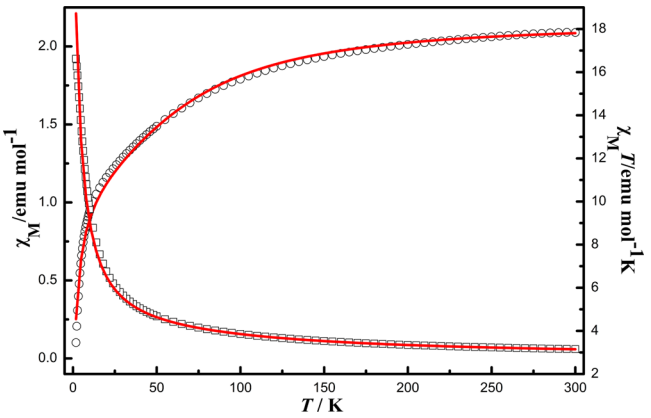

Figure 7. Temperature dependence of magnetic susceptibility in the forms of χ_MT and χ_M vs T for **2** at an applied field of 1000 Oe between 1.8 to 300 K. The red solid lines represent the best fitting results.

According to the crystal structure of **2**, the trimeric $\{Co_3\}$ cluster is significantly different from the linear trimer and triangular cluster documented,[9d,17] which can be linked by $COOH^-$ groups to produce the $\{Co_6\}$ dimers. Therefore, it is hard to model the magnetic behavior in the complicated system by deducing an exact expression including J parameter even if the orbital contribution of Co^{2+} ion is neglected. However, it can be confirmed by a poor fit to an equation for Co^{2+} ion with ground state of $^4T_{1g}$. Instead, the data can be well-fitted by using an expression $\chi_M = 6\chi_{Co}$ for $S = 3/2$ system with dominant ZFS effects.[22]

$$\chi_{\parallel} = \frac{Ng^2\beta^2}{kT}\frac{1 + 9e^{-2x}}{4(1 + e^{-2x})} \quad (3)$$

$$\chi_{\perp} = \frac{Ng^2\beta^2}{kT}\frac{4 + \frac{3}{x}(1 - e^{-2x})}{4(1 + e^{-2x})} \quad (4)$$

$$\chi' = \frac{\chi_{\parallel} + 2\chi_{\perp}}{3} \quad (5)$$

$$\chi_{Co} = \frac{\chi'}{1 - \left(\frac{2zJ'}{Ng^2\beta^2}\right)\chi'} \quad (6)$$

where g is the Lande value, $x = D/kT$, D is the magnitude of the ZFS, z is the number of neighbors, and J' is the magnitude of the intermolecular interactions. The best least-squares fit parameters are $g = 2.55$, $D = 74.06$ cm^{-1}, $zJ' = -1.19$ cm^{-1}, and $R = \sum[(\chi_MT)_{obsd} - (\chi_MT)_{calcd}]^2/\sum[(\chi_MT)_{obsd}]^2 = 4.29 \times 10^{-3}$, which further demonstrates that antiferromagnetic interaction exists between adjacent Co^{2+} ions, being in accordance with the previously reported value for $S = 3/2$ system with dominant ZFS effects.[22]

The field dependence of magnetization (M) for **1** and **2** was tested at 2 K in the range of 0–7 T (Supporting Information, Figure S8). The M values are 3.85 $N\mu_B$ for **1** and 12.23 $N\mu_B$ for **2**, which are far from the saturation values of 10 $N\mu_B$ for **1** and 18 $N\mu_B$ for **2**, respectively, further suggesting the presence of antiferromagnetic interactions between adjacent Mn^{2+} ions in **1** and Co^{2+} ions in **2**.[22]

To further study the dynamics of magnetization, the temperature dependence of the alternating-current (ac) magnetic susceptibilities for **1** and **2** are collected at zero dc fields. Unfortunately, no out-of-phase signal is detected in **1** and **2** (Supporting Information, Figure S9).

Gas Adsorption and Separation. Considering that **3** possesses vacant pores, we attempt to soak the crystals of **3** in the low-boiling point solvents so that the free DMF molecules can be exchanged. When soak the samples in CH_2Cl_2 for 3 d, the samples are crystalline. PXRD patterns show that the framework is retained before and after exchanging solvents, as well as the activated one and after the measure (Supporting Information, Figure S10).

The activated **3** only displays external surface adsorption of N_2 at 77 K. In contrast, CO_2 adsorption measured at 195 K exhibits a fully reversible type-I isotherm with a high CO_2 uptake (190 $cm^3\cdot g^{-1}$) at 0.15 bar; subsequently, this value slowly but steadily increases to 209 $cm^3\cdot g^{-1}$ at 1 bar, indicating

DOI: 10.1021/ic502488c
Inorg. Chem. 2015, 54, 586–595

that **3** possesses the microporous nature (Figure 8a).[23] The Brunauer–Emmett–Teller (S_{BET}) and Langmuir surface ($S_{Langmuir}$) areas of **3** based on the 195 K CO_2 adsorption data are 847 and 876 $m^2 \cdot g^{-1}$, respectively.

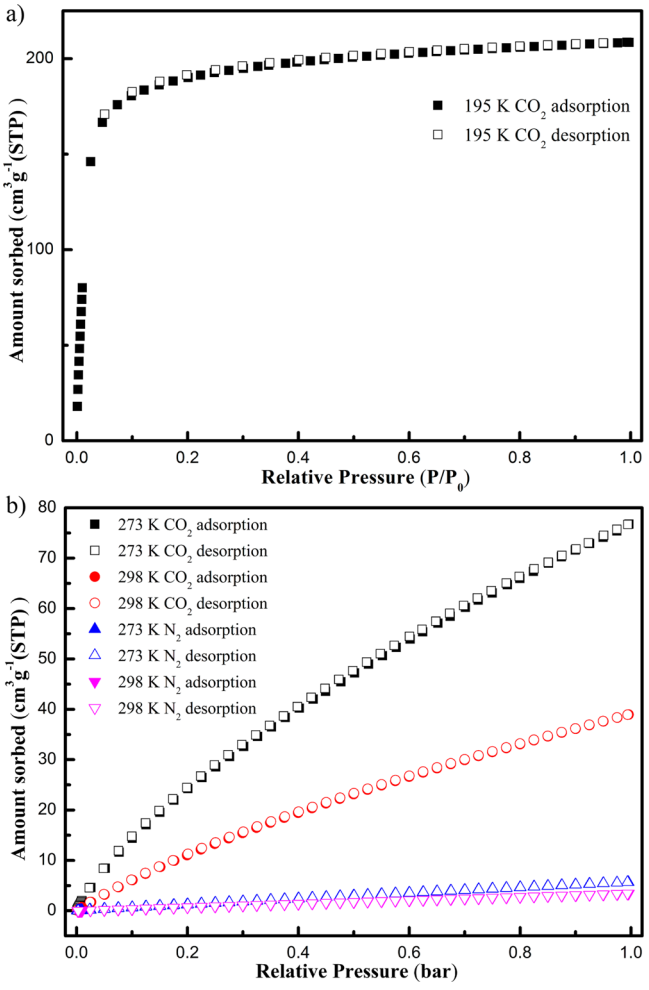

Figure 8. (a) Adsorption isotherms of **3** for CO_2 at 195 K (adsorption and desorption lines are presented with closed and open symbols, respectively). (b) Adsorption isotherms of **3** for CO_2 and N_2 at 273 and 298 K (adsorption and desorption lines are presented with closed and open symbols, respectively).

The CO_2 sorption measurements for **3** at 273 and 298 K are also completely reversible and show the steep rise at the low-pressure region with uptake of 76.8 (15.1%) and 39.0 $cm^3 \cdot g^{-1}$ (7.7%) at 1 bar, respectively (Figure 8b). Comparatively, the N_2 uptakes are 5.7 and 3.4 $cm^3 \cdot g^{-1}$ at 273 and 298 K (1 bar), respectively (Figure 8b). To better know these results, the adsorption enthalpies (Q_{st})[24] of CO_2 are counted from the adsorption data at 273 and 298 K by using both Clausius–Clapeyron equation and virial-type fitting method to quantitatively assess the binding strengths between CO_2 and the framework (Supporting Information, Figure S11). As expected, the Q_{st} values at zero coverage are 34.7 and 28.8 $kJ \cdot mol^{-1}$ calculated by Clausius–Clapeyron equation and virial-type fitting method for **3** (Figure 9a), suggesting strong interactions between CO_2 and the framework. Comparably high Q_{st} values have only been observed in few microporous materials.[2a,23]

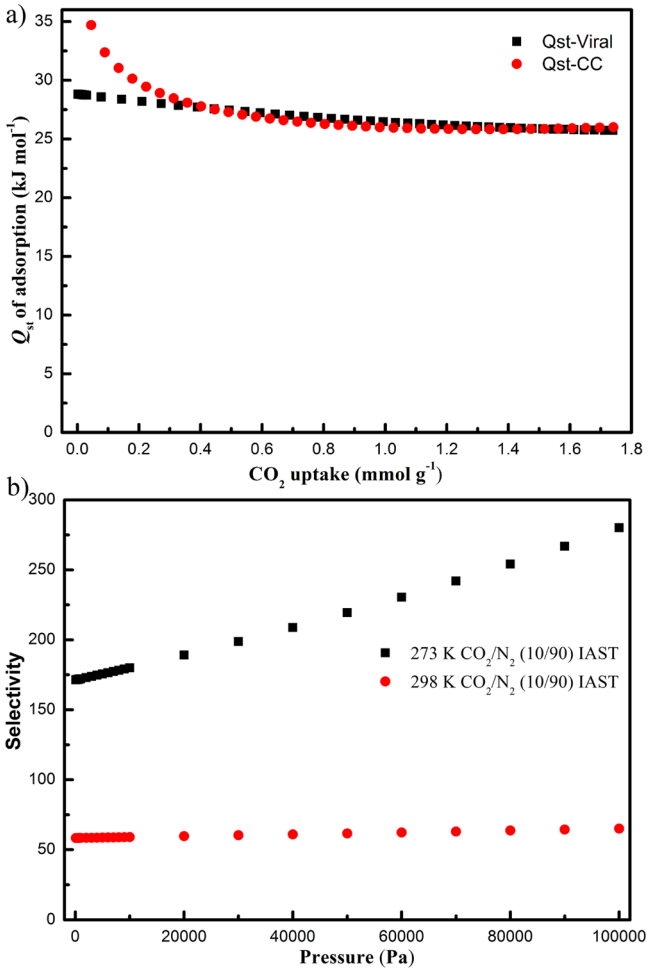

Figure 9. (a) The isosteric heats of CO_2 adsorption (Q_{st}) values are calculated by Clausius–Clapeyron equation and virial-type fitting method for **3**, respectively. (b) IAST calculated selectivity abilities of CO_2/N_2 (10/90) from 10/90 gas-phase CO_2 and N_2 mixtures based upon the experimental data of the pure gases at 273 and 298 K, respectively.

The gas-selective adsorption capacity in MOFs could be achieved from single-component sorption data.[2b,23] The CO_2/N_2 (10/90) selectivity abilities in a binary mixture would be required for practical utility; these abilities are calculated by employing IAST[14] method from the adsorption data of CO_2 and N_2 at 273 and 298 K (Supporting Information, Figure S12), respectively, as illustrated in Figure 9b. Calculated from the experimental data, the CO_2/N_2 selectivity abilities at zero coverage are approximately 171:1 and 58:1 at 273 and 298 K, respectively, which have obvious increases in the whole measured pressure range and achieve the maximum values at 1 bar with 280:1 and 65:1 at 273 and 298 K, respectively. To the best of our knowledge, such high CO_2/N_2 selectivity ability has only been observed for a small number of MOFs (Supporting Information TableS1),[2b,23] which suggests that the selective sorption ability of **3** is among the norm MOFs for probable applications in highly selective CO_2 adsorption and the separation of CO_2 from the mixtures of CO_2 and N_2.

CONCLUSIONS

In conclusion, five MOFs constructed by $\{M_n(CO_2)_4\}$-type SBUs and $abtc^{4-}$ ligands have been successfully synthesized via

DOI: 10.1021/ic502488c
Inorg. Chem. 2015, 54, 586–595

solvothermal method, and they exhibit four distinct architectures resulting from different coordinated modes of $abtc^{4-}$ ligands. **1** and **5** present the **PtS**-type 3D framework. Three independent Co^{2+} ions in **2** are bridged by $COOH^-$ groups to afford a scarce $\{Co_3\}$ cluster, which further are bridged by $abtc^{4-}$ ligands to present the 3D network with a new **ZSW1**-type topological structure. **3** exhibits the 3D **NbO**-type cage, and **4** displays the uncommon **nou**-type topological architecture. The solid-state luminescence properties of **1**−**5** have been examined. The variable-temperature magnetic susceptibility measurements reveal that dominant antiferromagnetic interactions exist in **1** and **2**. Meanwhile, **3** shows significant adsorption capability of CO_2 and highly selective sorption of CO_2 over N_2. Notice that the successful preparation of **1**−**5** illustrates the significant influence of reaction conditions (such as the species of metal centers, the rate of the reactants, the reaction temperature, and solvent) on structures. The work provides a promising pathway to rational design and preparation of MOFs with polycarboxylic ligands, and further effort is being devoted to construct functional MOFs with desired structures by other organic polycarboxylic ligands.

■ ASSOCIATED CONTENT

Supporting Information

Illustrations of metal ion coordination environments, plot indicating temperature dependence of magnetic susceptibility, PXRD patterns, TGA, spectroscopic characterizations, and magnetic and crystallographic data of MOFs **1**−**5**. Structures in CIF format. This material is available free of charge via the Internet at http://pubs.acs.org. CCDC Nos. 1013694−1013698 are for **1**−**5**, respectively. These data can be obtained free of charge from The Cambridge Crystallographic Data Centre via www.ccdc.cam.ac.uk/data_request/cif.

■ AUTHOR INFORMATION

Corresponding Author

* E-mail: pcheng@nankai.edu.cn. Fax: (+86) 22-23502458.

Notes

The authors declare no competing financial interest.

■ ACKNOWLEDGMENTS

This work was supported by the MOST ("973 program" 2012CB821702), the NSFC (21301099, 21421001), the MOE (IRT-13022, 13R30), 111 project (B12015), and the NSF of Tianjin (13JCZDJC32200).

■ REFERENCES

(1) (a) Zhou, H. C.; Kitagawa, S. *Chem. Soc. Rev.* **2014**, *43*, 5415−5418. and references therein (b) Zhou, H. C.; Long, J. R.; Yaghi, O. M. *Chem. Rev.* **2012**, *112*, 673−674 and references therein.

(2) (a) Sumida, K.; Rogow, D. L.; Mason, J. A.; McDonald, T. M.; Bloch, E. D.; Herm, Z. R.; Bae, T. H.; Long, J. R. *Chem. Rev.* **2012**, *112*, 724−781. (b) Li, J. R.; Sculley, J.; Zhou, H. C. *Chem. Rev.* **2012**, *112*, 869−932. (c) He, Y. B.; Zhou, W.; Qian, G. D.; Chen, B. L. *Chem. Soc. Rev.* **2014**, *43*, 5657−5678. (d) Gong, Y. N.; Meng, M.; Zhong, D. C.; Huang, Y. L.; Jiang, L.; Lu, T. B. *Chem. Commun.* **2012**, *48*, 12002−12004. (e) Huang, Y. L.; Gong, Y. N.; Jiang, L.; Lu, T. B. *Chem. Commun.* **2013**, *49*, 1753−1755.

(3) (a) Cui, Y. J.; Yue, Y. F.; Qian, G. D.; Chen, B. L. *Chem. Rev.* **2012**, *112*, 1126−1162. (b) Kreno, L. E.; Leong, K.; Farha, O. K.; Allendorf, M.; Van Duyne, R. P.; Hupp, J. T. *Chem. Rev.* **2012**, *112*, 1105−1125. (c) Hu, Z. C.; Deibert, B.J.; Li, J. *Chem. Soc. Rev.* **2014**, *43*, 5815−5840. (d) Gong, Y. N.; Lu, T. B. *Chem. Commun.* **2013**, *49*, 7711−7713. (e) Gong, Y. N.; Jiang, L.; Lu, T. B. *Chem. Commun.* **2013**, *49*, 11113−11115.

(4) Zhang, T.; Lin, W. B. *Chem. Soc. Rev.* **2014**, *43*, 5982−5993.

(5) Dechambenoit, P.; Long, J. R. *Chem. Soc. Rev.* **2011**, *40*, 3157−3181.

(6) Lee, Y. G.; Moon, H. R.; Cheon, Y. E.; Suh, M. P. *Angew. Chem., Int. Ed.* **2008**, *47*, 7741−7745.

(7) Yaghi, O. M.; O'Keeffe, M.; Ockwig, N. W.; Chae, H. K.; Eddaoudi, M.; Kim, J. *Nature.* **2003**, *423*, 705−714.

(8) (a) Bourne, S. A.; Lu, J. J.; Mondal, A.; Moulton, B.; Zaworotko, M. J. *Angew. Chem., Int. Ed.* **2001**, *40*, 2111−2113. (b) Chui, S. S. Y.; Lo, S. M. F.; Charmant, J. P. H.; Orpen, A. G.; Williams, I. D. *Science* **1999**, *283*, 1148−1150. (c) Wong-Foy, A. G.; Lebel, O.; Matzger, A. J. *J. Am. Chem. Soc.* **2007**, *129*, 15740−15741. (d) Yang, S. H.; Sun, J. L.; Ramirez-Cuesta, A. J.; Callear, S. K.; David, W. I. F.; Anderson, D. P.; Newby, R.; Blake, A. J.; Parker, J. E.; Tang, C. C.; Schröder, M. *Nat. Chem.* **2012**, *4*, 887−894.

(9) (a) Liu, Y. L.; Eubank, J. F.; Cairns, A. J.; Eckert, J.; Kravtsov, V. C.; Luebke, R.; Eddaoudi, M. *Angew. Chem., Int. Ed.* **2007**, *46*, 3278−3283. (b) Cairns, A. J.; Perman, J. A.; Wojtas, L.; Kravtsov, V. C.; Alkordi, M. H.; Eddaoudi, M.; Zaworotko, M. J. *J. Am. Chem. Soc.* **2008**, *130*, 1560−1561. (c) Wang, X. S.; Ma, S. Q.; Rauch, K.; Simmons, J. M.; Yuan, D. Q.; Wang, X. P.; Yildirim, T.; Cole, W. C.; López, J. J.; Meijere, A.; Zhou, H. C. *Chem. Mater.* **2008**, *20*, 3145−3152. (d) Zhao, J.; Li, D. S.; Ke, X. J.; Liu, B.; Zou, K.; Hu, H. M. *Dalton Trans.* **2012**, *41*, 2560−2563. (e) Xue, M.; Zhu, G. S.; Li, Y. X.; Zhao, X. J.; Jin, Z.; Kang, E. H.; Qiu, S. L. *Cryst. Growth Des.* **2008**, *8*, 2478−2483. (f) Yang, M.; Jiang, F. L.; Chen, Q. H.; Zhou, Y. F.; Feng, R.; Xiong, K. C.; Hong, M. C. *CrystEngComm* **2011**, *13*, 3971−3974. (g) Meng, M.; Zhong, D. C.; Lu, T. B. *CrystEngComm* **2011**, *13*, 6794−6800.

(10) Zhang, S. W.; Shi, W.; Li, L. L.; Duan, E. Y.; Cheng, P. *Inorg. Chem.* **2014**, *53*, 10340−10346.

(11) Ameerunisha, S.; Zacharias, P. S. *J. Chem. Soc., Perkin Trans.* **1995**, *2*, 1679−1682.

(12) (a) Sheldrick, G. M. *SHELXS97, Program for Crystal Structure Solution;* University of Göttingen: Göttingen, Germany, 1997;. (b) Sheldrick, G. M. *SHELXL97, Program for Crystal Structure Refinement;* University of Göttingen: Göttingen, Germany, 1997.

(13) (a) Spek, A. L. Utrecht University: Utrecht, The Netherlands, 1998. (b) Spek, A. L. *Acta Crystallogr.* **2009**, *D65*, 148−155.

(14) Myers, A. L.; Prausnitz, J. M. *AIChE J.* **1965**, *11*, 121−127.

(15) Brown, I. D.; Altermatt, D. *Acta Crystallogr.* **1985**, *B41*, 244−247.

(16) (a) Blatov, V. A.; Shevchenko A. P.; Proserpio, D. M. *Cryst. Growth Des.* **2014**, *14*, 3576−3586. TOPOS software available at http://www.topos.ssu.samara.ru. (b) O'Keeffe, M.; Yaghi O. M.; Ramsden, S. *Reticular Chemistry Structure Resourece;* 2007, database available at http://rcsr.anu.edu.au/.

(17) Wei, Y. S.; Chen, K. J.; Liao, P. Q.; Zhu, B. Y.; Lin, R. B.; Zhou, H. L.; Wang, B. Y.; Xue, W.; Zhang, J. P.; Chen, X. M. *Chem. Sci.* **2013**, *4*, 1539−1546.

(18) (a) Fliegl, H.; Kohn, A.; Hattig, C.; Ahlrichs, R. *J. Am. Chem. Soc.* **2003**, *125*, 9821−9827. (b) Bhattacharya, S.; Sanyal, U.; Natarajan, S. *Cryst. Growth Des.* **2011**, *11*, 735−747.

(19) Tan, X. S.; Sun, J.; Xiang, D. F.; Tang, W. X. *Inorg. Chim. Acta* **1997**, *255*, 157−161.

(20) Kahn, O. *Molecular Magnetism;* VCH: New York. 1993.

(21) Ginsberg, A. P.; Lines, M. E. *Inorg. Chem.* **1972**, *11*, 2289−2290.

(22) (a) Zou, J. Y.; Shi, W.; Zhang, J. Y.; He, Y. F.; Gao, H. L.; Cui, J. Z.; Cheng, P. *CrystEngComm* **2014**, *16*, 7133−7140. (b) Miyasaka, H.; Clérac, R.; Campos-Fernández, C. S.; Dunbar, K. R. *Inorg. Chem.* **2001**, *40*, 1663−1671. (c) Marshall, S. R.; Rheingold, A. L.; Dawe, L. N.; Shum, W. W.; Kitamura, C.; Miller, J. S. *Inorg. Chem.* **2002**, *41*, 3599−3601.

(23) (a) Li, B.; Wang, H. L.; Chen, B. L. *Chem.—Asian. J.* **2014**, *9*, 1474−1498 and references therein. (b) Nugent, P.; Belmabkhout, Y.; Burd, S. D.; Cairns, A. J.; Luebke, R.; Forrest, K.; Pham, T.; Ma, S. Q.; Space, B.; Wojtas, L.; Eddaoudi, M.; Zaworotko, M. J. *Nature* **2013**,

DOI: 10.1021/ic502488c
Inorg. Chem. 2015, 54, 586−595

495, 80−84. (c) McDonald, T. M.; Lee, W. R.; Mason, J. A.; Wiers, B. M.; Hong, C. S.; Long, J. R. *J. Am. Chem. Soc.* **2012**, *134*, 7056−7065. (d) Xiang, S. C.; He, Y. B.; Zhang, Z. J.; Wu, H.; Zhou, W.; Krishna, R.; Chen, B. L. *Nat. Commun.* **2012**, *3*, 954−963. (e) Choi, H. S.; Suh, M. P. *Angew. Chem., Int. Ed.* **2009**, *48*, 6865−6869. (h) Du, L. T.; Lu, Z. Y.; Zheng, K. Y.; Wang, J. Y.; Zheng, X.; Pan, Y.; You, X. Z.; Bai, J. F. *J. Am. Chem. Soc.* **2013**, *135*, 562−565. (f) Li, J. R.; Yu, J. M.; Lu, W. G.; Sun, L. B.; Sculley, J.; Balbuena, P. B.; Zhou, H. C. *Nat. Commun.* **2013**, *4*, 204−212.

(24) (a) Czepirski, L.; Jagiello, J. *Chem. Eng. Sci.* **1989**, *44*, 797−801. (b) Rowsell, J. L. C.; Yaghi, O. M. *J. Am. Chem. Soc.* **2006**, *128*, 1304−1315.

DOI: 10.1021/ic502488c
Inorg. Chem. 2015, 54, 586−595